RSC Advances

PAPER

View Article Online
View Journal | View Issue

Cite this: *RSC Adv.*, 2023, **13**, 21199

Simple fabrication of carbon quantum dots and activated carbon from waste wolfberry stems for detection and adsorption of copper ion†

Yunjia Xu,[a] Jingming Lan,[a] Baoying Wang,[a] Chunmiao Bo,[a] Junjie Ou[b] and Bolin Gong *[a]

Removal of heavy metal pollution is an endless topic, because heavy metals can cause irreversible damage to the human body and environment. It is urgent to develop novel materials for detection and adsorption of heavy metal ions. In this paper, waste wolfberry straw was utilized as a carbon source, and two simple methods were developed to successfully prepare activated carbon (AC) and carbon quantum dots (CQDs). The fabrication conditions were optimized by adjusting the mass ratio of precursor to activator, type of activator and activation times. When sodium hydroxide (NaOH) was selected as an activator (6 : 1, mass ratio of NaOH to AC-precursor), and the activation was performed at 600 °C for 1 h, the highest specific surface area of the obtained AC-NaOH-3 reached 3016 $m^2\ g^{-1}$. The adsorption capacity for copper ions (Cu^{2+}) reached 68.06 mg g^{-1}. The preparation conditions for CQDs were also optimized by adjusting the concentration of wolfberry stem, reaction time and temperature. When the wolfberry stem concentration was 7.5 g L^{-1}, and the activation was performed at 200 °C for 24 h, the obtained CQDs exhibited strong fluorescence emission in the blank and 12 kinds of metal ion solutions, respectively, however, the fluorescence intensity was remarkably decreased after adding Cu^{2+}. In the range of 10–80 nM, the linear correlation coefficient between the concentration of Cu^{2+} and fluorescence intensity of CQDs was 0.992, and the limit of detection was 2.83 nmol L^{-1}. Thus, these two kinds of materials were prepared from wolfberry stem, which opened up a new way for the application in adsorption and detection of copper ions.

Received 15th June 2023
Accepted 7th July 2023

DOI: 10.1039/d3ra04026g

rsc.li/rsc-advances

1 Introduction

The rapid development of industrialization has given rise to great pollution of the natural environment. Industrial wastewater is mainly discharged into rivers and lakes, producing a plethora of heavy metals.[1] Most heavy metals are difficult to degrade naturally, which has a significant impact on the natural ecosystem.[2,3] Copper ions (Cu^{2+}), a most common heavy metal ion, can be released into the environment through industrial and human activities. Once Cu^{2+} is taken into the human body and accumulates, it can cause health hazards and diseases such as liver failure and heart damage and even death. Therefore, sensitive detection methods and efficient adsorption materials are essential to prevent and reduce Cu^{2+} pollution of the environment.[4,5]

There are many approaches of heavy metal removal, such as ion exchange, electrochemical method, adsorption, *etc.*[6–9] Recently, Hosseini and his colleagues[10] prepared a novel layer-by-layer (LbL) cation exchange membrane by coating a chitosan-nano activated carbon layer on a polyvinyl chloride based heterophase cation exchange membrane. The experiments showed that the LBL membrane has a good ability to remove heavy metal ions such as Cu^{2+}, Ni^{2+}, and Pb^{2+}. Abdelhamid *et al.*[11] used sheet former Rapid-Köthen (R. K.) to process hierarchical porous zeolitic imidazolate frameworks (ZIF-8) into cellulose paper-based materials to achieve satisfactory adsorption and electrochemical detection of metal ions such as Pb^{2+}, Fe^{3+} and Cu^{2+}. The adsorption and electrochemical detection of Pb^{2+}, Fe^{3+} and Cu^{2+} were obtained with satisfactory adsorption capacity and low electrochemical detection limits. According to relevant reports,[12,13] in most situations, adsorption is the most effective method. In contrast, other methods have obvious disadvantages, such as the generation of large amounts of sludge, low treatment quality, harsh operating conditions and too high costs. Adsorption is a better method for wastewater treatment. Due to its versatility in design, reversibility and high

[a]School of Chemistry and Chemical Engineering, Key Laboratory for Chemical Engineering and Technology, State Ethnic Affairs Commission, North Minzu University, Yinchuan, 750021, China. E-mail: gongbolin@163.com

[b]State Key Laboratory of Synthetic and Natural Functional Molecule Chemistry of Ministry of Education, College of Chemistry & Materials Science, Northwest University, Xi'an 710127, China

† Electronic supplementary information (ESI) available. See DOI: https://doi.org/10.1039/d3ra04026g

quality wastewater treatment, it is the preferred choice for heavy metals removal.[14] Activated carbon (AC) is a traditional adsorption material. On the hand, biomass is a promising source of carbon for the preparation of AC, because the biowastes from agriculture can be recycled so that the economy can be saved and the environment can be protected.[15] On the other hand, detecting heavy metals in the environment is also essential to controlling heavy metal pollution. There are several detection methods by using UV-vis spectrophotometry, ion exchange chromatography, flame atomic absorption spectrophotometry and so on.[16] However, they generally require high instrumental costs and complicated detection operations. Therefore, metal ion sensor platforms have received much attention in recent years, for instance, organic molecules, nanoparticles and carbon dots (CQDs). CQDs, as a kind of novel carbon nanomaterials, have attracted great attention since their discovery in 2004, due to their excellent hydrophilicity, biocompatibility, high electrical conductivity, low toxicity and controlled fluorescence property.[17] Licona-Aguilar *et al.* synthesized AC with sugarcane bagasse and orange peel as raw materials in acidic medium (H_3PO_4, 85 wt%) employing a physicochemical activation method. The prepared AC could remove 94% of Pb^{2+} and 85.1% of Cu^{2+}.[18] Malti *et al.* utilized citrus Sinensis peel as a carbon source and H_2O_2 as an activator to prepare biochar and achieved a maximum theoretical adsorption capacity of 11.36 mg g^{-1} of Cu^{2+} in water.[19] Zhu *et al.*[17] synthesized fluorescent CQDs by a simple two-step method with biomass lignin as the carbon source, which had a significant selective fluorescence quenching effect on Fe^{3+}. These researches offer us hints to fabricate more functional materials of AC or CQDs with biomass resources.

Chinese wolfberry is abundantly distributed in Ningxia, Qinghai and Xinjiang Province, China. Amongst others, wolfberry can be used as raw material to obtain nitrogen doped carbon quantum dots (N-CQD) by green preparation methods. These N-CQDs have been developed as a highly sensitive fluorescent 'on–off' switch sensor for the detection of Fe^{3+} and L-ascorbic acid. Wolfberry stems as a by-product of wolfberry has never been used in a rational and high value way.[20] In this work, both fluorescent CQDs and biomass AC with high specific surface area were fabricated with wolfberry stems as carbon source, which can offer an alternative to wastewater treatment, as shown in Fig. 1. The obtained CQDs were applied in ultrasensitive detection of Cu^{2+}, while AC could be utilized for adsorption of copper ions.

2 Experiment

2.1 Materials

KOH, NaOH and $ZnCl_2$ were provided by Aladdin Industries (Shanghai) Co., Ltd. Standard solutions of metal ions (Li^+, Cd^{2+}, Co^{2+}, Zn^{2+}, Ca^{2+}, Cr^{3+}, Cu^{2+}, Fe^{3+}, K^+, Mg^{2+}, Na^+, and Zr^{4+}) were prepared with ultrapure water from respective metal salts of $ZnCl_2$, $CaCl_2$, LiCl, $Cd(NO_3)_2 \cdot 4H_2O$, $CoCl_2 \cdot 6H_2O$, $Cr(NO_3)_3 \cdot 9H_2O$, $CuSO_4 \cdot 5H_2O$, $FeCl_3 \cdot 6H_2O$, KCl, $Mg(NO_3)_2$, NaCl and $ZrCl_4$, which were also from Aladdin Industries (Shanghai) Co., Ltd. HCl, quinine sulfate and ethanol were provided by Sinopharm Chemical Reagent Co., Ltd. Wolfberry stem was provided by Ningxia Academy of Agricultural Sciences (Yinchuan, China). The above reagents are of analytical purity and have not been processed.

2.2 Preparation of AC

The AC was prepared by a two-step method. In short, the dried wolfberry stem was cleaned, crushed and passed through a sieve. The crushed wolfberry stems (5 g) were carbonization at 600 °C under a stream of N_2 to obtain the carbonation products (AC-precursor ≈ 1.2 g), which was then mixed with activators (NaOH, $ZnCl_2$, KOH) at various mass ratios (1 : 1, 1 : 2, 1 : 4, 1 : 6). The activation was performed under N_2 stream at high temperature (400–800 °C). After the activation was over, the product was washed with HCl and water to neutral, and finally dried in an oven to acquire biomass AC. For the sake of subsequent discussion. Named according to different qualities as (AC-NaOH-1–4, AC-$ZnCl_2$-1–4, AC-KOH, 1–4). Named according to different preparation conditions as (AC-NaOH-5–10).

2.3 Preparation of CQDs

The powdered wolfberry stem was put into a reaction kettle with 60 mL of aqueous ethanol solution (v/v, 1/1). After heating the oven to 200 °C, it was subsequently placed and maintained at

Fig. 1 Schematic preparation of CQDs and AC from wolfberry stem.

that temperature for 24 h. Following this, it was cooled to room temperature and then removed. A yellow suspension was obtained by centrifugation, and the liquid was filtered through a 0.22 μm microporous membrane to remove insoluble impurities. The CQDs solution was then dialyzed with a dialysis membrane (1000 Da) for 24 h. The obtained CQDs were stored at 4 °C for further assays.

2.4 Characterization of AC and CQDs

AC and CQDs were characterized by FTIR ranging from 4000 to 400 cm^{-1} (Thermo Nicolet iS50 spectrometer (Nicolet, Wisconsin, USA)), SEM images were obtained using a JSM-6480LV at 5.0 kV. FEI Tecnai G2 F20 transmission electron microscope (TEM) equipped with field emission source operating at 300 kV was used to record TEM images, X-ray photoelectron spectroscopy (XPS) (ESCALAB 250XI) and the C 1s line at 284.8 eV was used as the binding energy reference, ultraviolet visible data measured by SDPTOP UV2800S UV spectrophotometer, the XRD test was measured by a Rigaku D/MAX-2550 X-ray diffractometer, in Japan. Cu Ka radiation source (l = 0.154 nm), Ni filter, tube voltage 40 kV, tube current 450 mA, scan range $2q$ = 5–80°, continuous scan rate 0.02 min^{-1}, and data were collected automatically by computer. Fluorescence data were measured on an RF-5301PC fluorescence spectrophotometer in the excitation wavelength range of 300–380 nm and emission wavelength range of 320–600 nm with a fixed slit of 5 nm and adsorption experiments were performed on a thermostatic shaker (ZQP-75G, China) with 200 rpm shaking. The specific surface area of the material was analyzed with ASAP2020HD88 automatic specific surface area and micropore pore analysis (Max, USA) All samples were processed at 120 °C and 1.33 Pa for about 6 h for determination, and then air adsorption/desorption experiments were performed at liquid nitrogen temperature.

2.5 Fluorescent detection of Cu^{2+} by CQDs in aqueous solution

Sensitivity and selectivity are prerequisites for determining the fluorescent CQDs materials. To study the fluorescence selectivity of CQDs, 1 mL of CQDs suspensions and 4 mL of 12 metal ions solution were mixed and equilibration 5 min, and three measurements at 436 nm were taken and the average fluorescence intensity was recorded. Other measurements including isothermal and kinetic adsorption experiments were given in ESI.†

3 Results and discussion

3.1 Preparation and characterization of Wolfberry stem derived AC

AC is usually prepared by a two-step process, consisting of carbonization and activation. Of these, activation is an important preparation step that directly changes the pore structure of AC as well as the content of the surface functional groups, so choosing a suitable activator is a key step in the successful manufacture of AC. Therefore, three kinds of activators (NaOH, KOH and $ZnCl_2$) were chosen in our experiments. To screen the optimal conditions, this study measured the specific surface area, total pore volume, and pore width of AC by nitrogen adsorption–desorption method. The detailed results are summarized in Table 1.

AC-precursor is the product of carbonization from wolfberry stem, which exhibited a specific surface area of 245 $m^2 g^{-1}$, pore volume of 0.13 $cm^3 g^{-1}$, and micropore volume of only 0.07 $cm^3 g^{-1}$. After activation with NaOH, KOH or $ZnCl_2$, the products were achieved under the same conditions and assigned as AC-NaOH-(1–4), AC-KOH-(1–4), and AC-$ZnCl_2$-(1–4), respectively. Both alkaline activators had significant effects, and the specific surface area of the prepared AC increased gradually with an increase of the mass ratio of activator to precursor (AC-precursor). The specific surface area increased from 737 $m^2 g^{-1}$ to 2253 $m^2 g^{-1}$, when the mass ratio of NaOH to AC-precursor was increased from 1 : 1 (AC-NaOH-1) to 4 : 1 (AC-NaOH-3). The highest specific surface area of AC-NaOH-4 reached 3016 $m^2 g^{-1}$, the pore volume reached 1.54 $cm^3 g^{-1}$, while the micropore volume reached 0.74 $cm^3 g^{-1}$. The specific surface area slightly increased to 328 $m^2 g^{-1}$ after activation with the ratio of KOH to AC-precursor of 1 : 1 (AC-KOH-1), and the activation effect reached the most effective when the ratio of activator to AC-precursor was increased to 4 : 1 (AC-KOH-3), exhibiting high specific surface area of 2102 $m^2 g^{-1}$. However, further increasing the ratio of activator to AC-precursor (6 : 1), the specific surface area decreased to 1459 $m^2 g^{-1}$ (AC-KOH-4). So too much activator could not fully activate the AC-precursor. Both ACs possessed mainly microporous structure after activation, and the microporosity occupied more than 50% of total pore volume. Obviously, KOH was more alkaline and corrosive than NaOH, and the physical structure of AC was seriously destroyed during the activation process. $ZnCl_2$, as common activator, did not affect the material in this study. There was a decrease of specific surface area down to 32 $m^2 g^{-1}$. As a result, the final activation effect is significantly influenced by the use of different activators. $ZnCl_2$ as neutral salt has little effect on this study, while NaOH owns the strongest activation ability.

Activation temperature and time are essential factors in determining final physical structure of AC. The effects of activation temperature and time on properties of AC were investigated, as shown in Table 1. At 400 °C, the specific surface area was only 17 $m^2 g^{-1}$ (AC-NaOH-5) because the temperature was too low for NaOH to achieve activation. When the temperature was increased to 500 °C, the specific surface area reached 641 $m^2 g^{-1}$ (AC-NaOH-6), and when the temperature was increased to 600 °C, the maximum specific surface area of 2253 $m^2 g^{-1}$ (AC-NaOH-3). When the temperature further rose to relatively high temperature of 700 °C (AC-NaOH-9) or 800 °C (AC-NaOH-10), their physical structure was destroyed, resulting in decrease of specific surface area (1935 or 1899 $m^2 g^{-1}$) and pore volume (1.20 or 1.16 $cm^3 g^{-1}$). The activation time is an important factor for affecting micropores and mesopores of AC. When the activation time was 30 min, the specific surface area of AC-NaOH-7 was 1471 $m^2 g^{-1}$, the pore volume was 0.78 $cm^3 g^{-1}$, in which the micropore volume of 0.51 $cm^3 g^{-1}$ occupied 65% of the total pore volume. With an extension of activation

Table 1 Physical properties of AC obtained with different conditions

	Preparation condition (°C-min)	S_{BET} ($m^2\ g^{-1}$)	S_{mic} ($m^2\ g^{-1}$)	V_p ($cm^3\ g^{-1}$)	V_{mic} ($cm^3\ g^{-1}$)	Pore size (nm)
AC-precursor	600-60	245	141	0.13	0.07	3.46
AC-NaOH-1	600-60	737	507	0.40	0.25	3.48
AC-NaOH-2	600-60	1197	915	0.64	0.45	3.64
AC-NaOH-3	600-60	2253	1364	1.15	0.67	3.18
AC-NaOH-4	600-60	3016	1509	1.54	0.74	2.97
AC-$ZnCl_2$-1	600-60	5	—	0.01	—	11.3
AC-$ZnCl_2$-2	600-60	6	—	0.01	—	10.5
AC-$ZnCl_2$-3	600-60	11	—	0.01	—	7.90
AC-$ZnCl_2$-4	600-60	32	—	0.05	—	7.80
AC-KOH-1	600-60	328	166	0.18	0.07	3.41
AC-KOH-2	600-60	388	282	0.24	0.13	4.93
AC-KOH-3	600-60	2102	1305	1.12	0.64	3.64
AC-KOH-4	600-60	1459	875	0.75	0.43	2.71
AC-NaOH-5	400-60	17	—	0.02	—	6.42
AC-NaOH-6	500-60	641	545	0.33	0.26	3.77
AC-NaOH-7	600-30	1471	1046	0.78	0.51	3.38
AC-NaOH-8	600-180	1584	801	0.88	0.39	3.32
AC-NaOH-9	700-60	1935	590	1.20	0.27	4.35
AC-NaOH-10	800-60	1899	172	1.16	0.05	3.40

time to 60 min, the specific surface area of AC-NaOH-3 reached 2253 $m^2\ g^{-1}$, and a micropore volume of 0.67 $cm^3\ g^{-1}$ occupied 58% of the total pore volume (1.15 $cm^3\ g^{-1}$). Further extension of activation time, the specific surface area of AC-NaOH-8 was 1584 $m^2\ g^{-1}$, and the micropore volume was 0.39 $cm^3\ g^{-1}$, which occupied 44% of total pore volume (0.88 $cm^3\ g^{-1}$). Thus, the optimal activation time was 1 h and the activation temperature was 600 °C.

Some materials are listed in Table S1.† Oss *et al.*[21] selected microalgae biomass produced in wastewater treatment plants as a precursor to produce AC, and obtained a specific surface area of 785 $m^2\ g^{-1}$ by activation at 800 °C for 160 min. Termite biodiesel could also be prepared as alternative carbon source using KOH as an activator at 900 °C for 9 h. The specific surface area of as-obtained AC was 1465 $m^2\ g^{-1}$.[22] A. Alazmi *et al.*[23] prepared an AC with a specific surface area of 2344 $m^2\ g^{-1}$ after activation by CO_2 applied palm seeds as carbon source. The specific surface area of the AC-NaOH-4 prepared in this study was 3016 $m^2\ g^{-1}$ after activation with NaOH at 600 °C. In comparison with the physical and chemical activation described above, the AC produced in our case exhibited higher surface area.

The adsorption characteristics of AC and its adsorption effect in actual water samples were studied. The specific operation is as follows: the common metal ions in Cu^{2+}, Fe^{3+}, Cr^{6+}, K^+, Na^+, Ca^{2+} are added to domestic water. The adsorption capacity is calculated according to formula S1.† The results are shown in Table S5.† AC showed excellent adsorption capacity and extensive adsorption properties.

Fig. S1a and b† shows the N_2 adsorption–desorption isotherms and pore size distribution of AC-NaOH-3 and AC-NaOH-4. It was noteworthy that the remarkable microporous property of AC exhibited type I isotherms, which was related to the enhanced adsorbent–adsorbent interactions in the narrow micropores, which leads to microporous filling at relative external pressures. The XRD of AC-NaOH-3 and AC-NaOH-4 are shown in Fig. S2a.† There was a broad diffraction peak at 23°, indicating a partially graphite crystal structure. The relatively weak peak at 44° corresponding to the crystalline plane was considered to be a honeycomb structure hybridized by sp^2 hybridization.[24] The other sharp peaks indicated impurities in the crystalline carbon or sodium residues in the active microporous carbon.

AC surface functional groups characterized by FTIR, and Fig. S2b†-AC presents the FT-IR spectrum of AC-NaOH-4. A broad peak of 3430 cm^{-1} appeared, which was related to the O–H stretching vibration of hydroxyl group and stretching vibration of amine group (N–H). The peak at 1534 cm^{-1} was attributed to C=O stretching vibrations, the peak at 1022 cm^{-1} was assigned to the bending absorption of C–O–C. Thus, the presence of these functional groups would enhance the adsorption of Cu^{2+}.[25] Fig. S3† shows SEM images of the untreated wolfberry stems Fig. S3a and b† and the treated products AC-NaOH-3 and AC-NaOH-4 Fig. S3c and d.† The untreated wolfberry stems rods appear to be smooth rod-like structures on the surface, however the surfaces of both carbon materials after this activation out a large number of porous pore structures, forming an ordered porous AC.

3.2 Adsorption ability of wolfberry stem derived AC for Cu^{2+}

To evaluate the adsorption capacity of AC on Cu^{2+}, we selected AC-NaOH-3 and AC-NaOH-4 as adsorbent materials. The adsorption capacity was calculated by eqn S1.† As shown in Fig. 2a, the adsorption equilibrium increased with an increase of Cu^{2+} concentration. Both ACs (AC-NaOH-3 and AC-NaOH-4) showed excellent adsorption with capacities of 50.21 and 68.06 mg g^{-1} respectively.

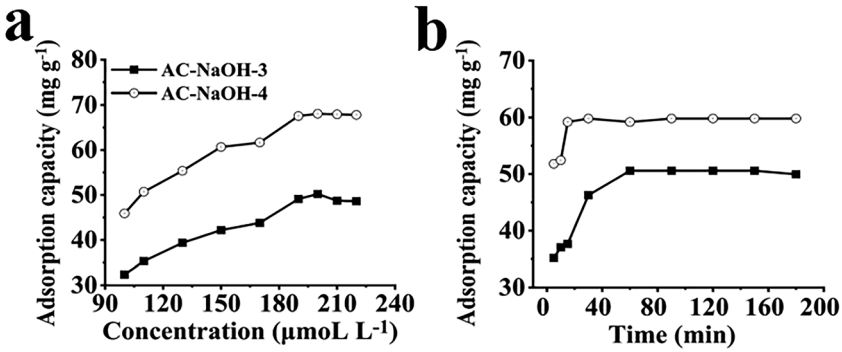

Fig. 2 (a) Isotherm adsorption and (b) dynamic adsorption of Cu^{2+} by AC-NaOH-3 and AC-NaOH-4.

Both the Langmuir and Freundlich models were calculated and fitted with eqn S2 and S3.† The relationship between C_e and Q_e was explored to establish the Langmuir isotherm, and the relationship between $\log C_e$ and $\log Q_e$ was also explored to establish the Freundlich isotherm. The result is shown in Fig. S4a, b and Table S2.† The R values of the Langmuir isotherm model for AC-NaOH-3 and AC-NaOH-4 were 0.981 and 0.993, which were higher than those of the Freundlich isotherm model (0.965 and 0.975). The results showed that the adsorption process of AC was more consistent with the Langmuir isotherm model, indicating that the adsorption of Cu^{2+} by AC was monolayer adsorption, which was similar with other AC.[26,27]

The time of adsorption equilibrium is also an important index to evaluate the adsorption performance, so the adsorption kinetic process is investigated, as shown in Fig. 2b. The adsorption capacity of NaOH-AC-3 reached equilibrium of 50.58 mg g^{-1} after 60 min, while AC-NaOH-4 reached equilibrium after 30 min of contact with an adsorption capacity of 59.81 mg g^{-1}. In order to investigate the rate of control steps and adsorption mechanisms of the AC adsorption process, pseudo-first-order and pseudo-second-order models were fitted and calculated by eqn S4 and S5.† So, two kinetic fitting results are presented in Fig. S4c, d and Table S3.† The linear correlation coefficients of the pseudo-second-order kinetic models for both AC ($R = 0.999$) were much higher than those of the pseudo-first-order kinetic models ($R = 0.566$, $R = 0.754$), confirming the applicability of the pseudo-second-order kinetic model to the observed adsorption behavior. The adsorption may be related to the functional groups and structure of the material. As mentioned above, the surfaces of AC-NaOH-3 and AC-NaOH-4 contained functional groups such as amino group ($-NH_2$), hydroxyl group (–OH) which provide chelating sites for Cu^{2+}, AC-NaOH-4 possessed larger specific surface area and pore volume. Therefore, AC-NaOH-4 could rapidly adsorb Cu^{2+} capacity in solution, indicating that AC has the ability to rapidly process Cu^{2+} in water.[28,29]

Calculated by eqn S6, as shown in Fig. S4e,† the segmental fit of the intraparticle diffusion model shows that the mass transfer process was characterized by a three-step control of adsorption rate. These three segments represent the thin film diffusion, mesoporous, and micropore diffusion processes. During the fast adsorption stage, the gradual increase in Cu^{2+} adsorption is attributed to the diffusion of Cu^{2+} in the pores of the adsorbent, which is an external diffusion-controlled process. The adsorption rates of three stages are $k_{id1} > k_{id2} > k_{id3}$, and the boundary thickness gradually increased during the adsorption process.[30,31] In the internal diffusion stage, the adsorption process consists of two stages, a short initial phase characterized by a higher slope and external diffusion phase with lower slopes corresponding to internal diffusion. This suggests that the adsorption of Cu^{2+} on the adsorbent is a result of the adsorbent being a combination of external diffusion and internal particle diffusion. The adsorption capacities of other ACs were also shown in Table S4.† Guo *et al.*[32] prepared AC from wheat straw by chemical activation using carbon disulfide was used to modify WS by a facile grafting method through epichlorohydrin and ethylenediamine. Then, it was used as an adsorbent for the removal of Cu^{2+} from aqueous solution with a capacity of 57.5 mg g^{-1} at 200 min. Wu *et al.*[33] prepared AC from Walnut shell to adsorb Cu^{2+} in aqueous polymetallic solutions with a capacity of 32 mg g^{-1} at 40 min. The maximum adsorption capacity of AC prepared from Pinewood as carbon source with H_3PO_4 as activator was 20 mg g^{-1} at 20 min.[29] AC-NaOH-4 could reach an adsorption capacity of 59 mg g^{-1}, indicating the ability to rapidly adsorb Cu^{2+} from solution and higher adsorption capacity.

3.3 Preparation and characterization of CQDs from wolfberry stem

3.3.1 Effects of preparation conditions on QY. Relative QY is important parameter for assessing the ability to convert fluorescence. Therefore, the relative QY of CQDs was estimated according to different preparation methods, QY was calculated by eqn S7†.[34,35] Quinine sulfate with similar excitation and emission wavelengths as CQDs was selected as the standard reference. The absorbance of CQDs and quinine sulfate was measured at the corresponding excitation wavelength.

The effect of reaction time, hydrothermal temperature and wolfberry stem adding concentration on the relative QY were investigated, as shown in Fig. 3. Three aspects were studied to investigate the reaction time (8–36 h) and temperature (80–240 °C), and Wolfberry stem adding concentration (1.25–37.5 g L^{-1}). The relative QY increased from 22% to 59% when the additive

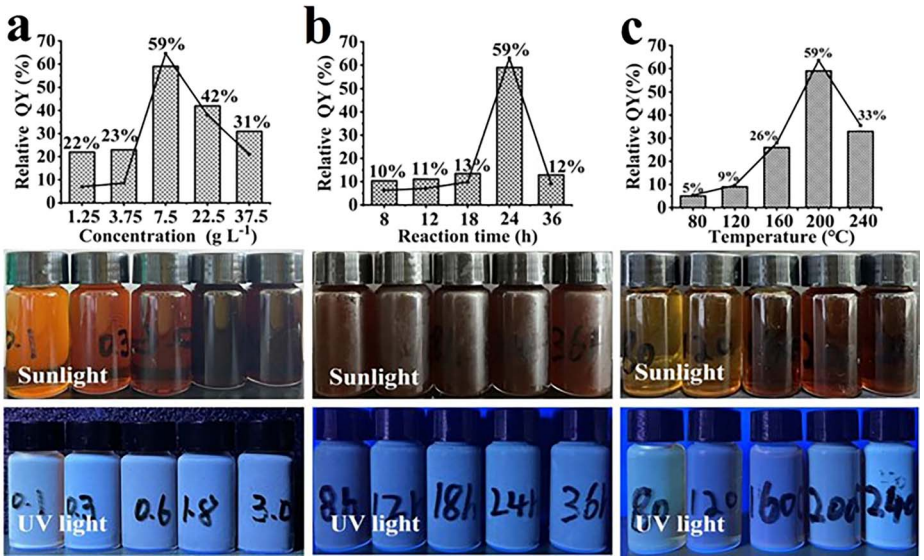

Fig. 3 Relative QY and images of CQDs under sunlight and UV irradiation under different preparation conditions. (a) Wolfberry stem concentration (1.25–37.5 g L^{-1}), (b) reaction time (8 to 36 h), (c) temperature (80 to 240 °C).

was increased from 1.25 to 7.5 g L^{-1}. The relative QY decreased to 43% and 31% after increasing the wolfberry stem adding concentration to 22.5 and 37.5 g L^{-1}. The relative QY increased from 10% to 59% at the reaction time (8 to 24 h) and decreased to 12% after extending the reaction time to 36 h. When the hydrothermal temperature was increased from 80 to 240 °C, the relative QY of CQDs also gradually increased to 33%. At shorter heating time and lower hydrothermal temperature, wolfberry stem did not decompose sufficiently in the reaction kettle, resulting in the incomplete formation of CQDs.[36] Therefore, the optimal condition of CQDs included the hydrothermal temperature of 200 °C, heating time of 24 h and adding wolfberry stem concentration of 7.5 g L^{-1}.

3.3.2 Morphological and optical properties of CQDs. CQDs were prepared by the hydrothermal method of wolfberry stem. It is well known that natural biomass molecules are held together by various chemical bonds. The breaking of chemical bonds, such as hydrogen bonds, provides an excellent incentive to degrade natural biomass into oligomers and microscopic molecules, which contain carboxyl groups, resulting in an acidic solution. The amorphous carbohydrates are further degraded under the conditions of acidity, high temperature and pressure to produce more water-soluble small molecules.[37] In the context of high temperature and pressure, small molecules dispersed within an ethanol solution undergo a substantial degree of sp^2 hybridization reactions, coupled with carbonization and passivation processes, culminating in the generation of carbon quantum dots at the nano-scale level.[38]

To confirm the structural characteristics of CQDs, the resulting products were analyzed by a series of tests, such as FTIR, XPS and TEM. As shown in Fig. 4a, the peak at 1706 cm^{-1} was assigned to the stretching vibration of C=C, while the strong peak at 1115 cm^{-1} was the deformation vibration of C–H was. Besides, the peaks at 3425, 1706, 1509 and 1215 cm^{-1} manifest the existence of –OH, C=O, C–N and C–O functional groups on the surface of CQDs.[39,40] The functional groups of CQDs were further characterized by XPS. The C 1s spectrum is shown in Fig. 4b, a strong C=C peak was located at 284.2 eV, and significant C–O and C=O peaks at 285.7 and 286.4 eV. In the O 1s spectrum (Fig. 4c), two peaks at 531.35 and 533.75 eV was the presence of C=O and C–OH. In the N 1s spectrum (Fig. 4d), three N atom structures, C–N–C (399.3 eV), amine-N (400.1 eV) and graphite-N (400.8 eV), emerged.[41] The morphology of synthesized CQDs could be clearly observed in the TEM images (Fig. 5). The zero-dimensional discrete quasi-spherical nanoparticles were produced, whose particle size was in the range of 1.7–2.5 nm.

The spectra of CQDs at different excitation wavelengths are shown in Fig. 6a. The maximum luminescence peak of the CQDs was concentrated at 436 nm and 360 nm excitation wavelength. In addition, as the excitation wavelength increases from 300 nm to 380 nm, the emission wavelength slowly shifted to red. This excitation-related behavior can be explained by the difference in particle size and emission trap location on each CQDs. As shown in Fig. 6b, the CQDs solution emitted blue fluorescence under UV light. As shown in Fig. 6c, UV-vis absorption spectra of CQDs showed two significant excitation adsorption bands located around 300 nm and 400 nm, respectively, with an optical adsorption edge. The absorption peak at 300 nm appeared due to a π–π* jump, which implies the formation of a conjugated backbone in CQDs. The weak adsorption shoulders below 460 nm was assigned to heteroatom-doped surface states or energy traps, which caused by n–π* leaps of functional groups.[42] The lifetime decay of CQDs (Fig. 6d) indicated a tri-exponential decay with average lifetime of 1.06 ns.

The stability of CQDs is an essential factor to evaluate these materials, and the effects of ionic strength, pH, and solvent on fluorescence intensity were investigated at an excitation wavelength of 360 nm. Fig. 7a shows that the fluorescent intense light

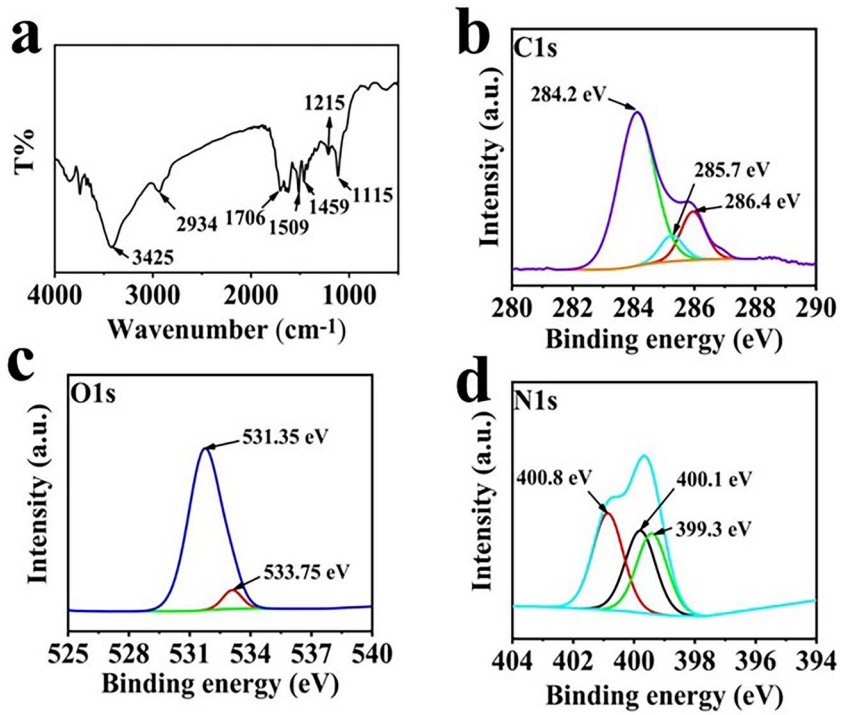

Fig. 4 (a) FT-IR of CQDs, (b) C 1s, (c) O 1s, (d) N 1s of XPS spectra of CQDs.

remains almost constant even when the NaCl concentration reaches 100 mmol L^{-1}. This result was consistent with other researches on the characteristics of fluorescent CQDs.[43] Under different pH conditions, as shown in Fig. 7b, the fluorescence intensity stabilized from pH 3.0 to 9.0, band then gradually decreased with further increase of pH. When the pH was 2.0, the fluorescence decreased, and over-protonation decreased fluorescence emission. However, the protonation\deprotonation of carboxyl groups gradually decreased as the solution pH increased to 9. As a result of deprotonation, the net surface charge was reduced, leading to further aggregation at high pH conditions and a reduce of fluorescence. The pH effect of fluorescence suggested that the CQDs microstructure was related to the source of blue fluorescence, and the site was prone to hydrogen bonding of the functional groups –OH and –COOH on the CQDs surface under acidic conditions, and thus the CQDs aggregates led to

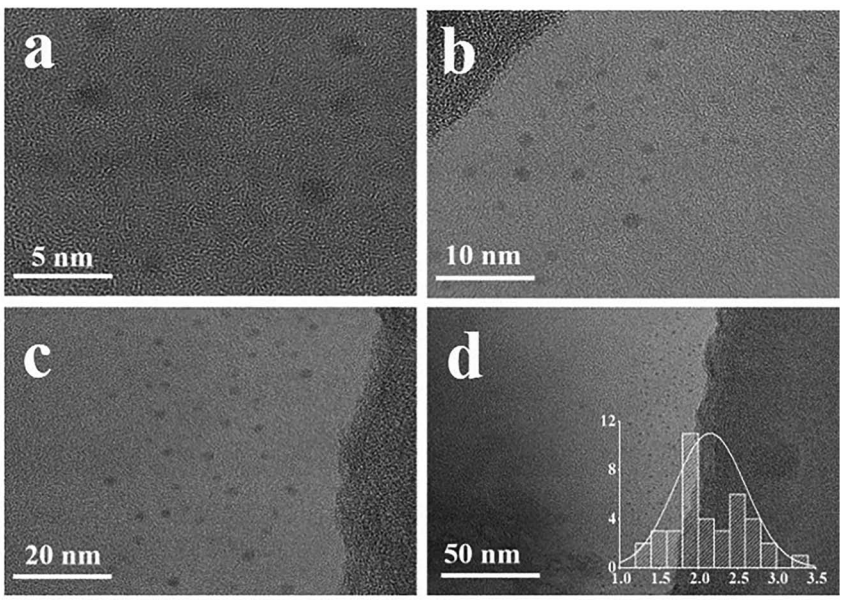

Fig. 5 TEM images and particle size distribution of CQDs.

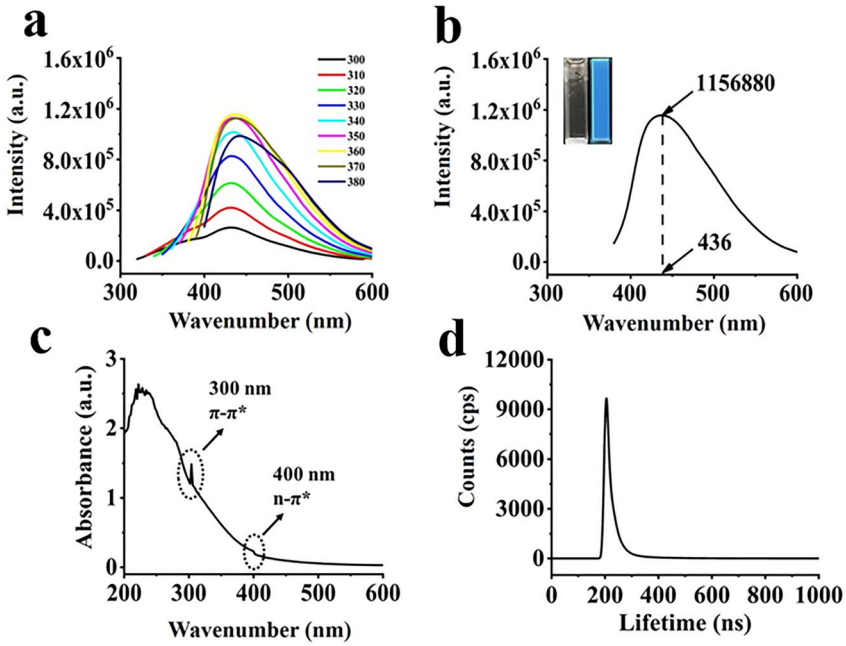

Fig. 6 (a) Photoluminescence emission spectra of various incident light excitations gradually increasing, (b) intense excitation spectra of CQDs, (c) UV-vis absorption spectra of aqueous solutions of CQDs, and (d) lifetime decay of CQDs.

fluorescence quenching.[44–46] Most CQDs are affected by solvents, so the fluorescence of CQDs was tested in toluene, petroleum ether, water, acetone, methanol and ethanol. As shown in Fig. 7c, CQDs exhibited good compatibility with water, ethanol, acetone, methanol and ethanol. Additionally, CQDs possessed the highest fluorescence intensity in aqueous solution (Fig. 7d). It should be related to a large number of –OH and –COOH groups on the surface of CQDs.

3.4 Fluorescent selective and sensitive detection by CQDs

The selectivity of CQDs for metal ions is essential and the fluorescence intensity of the metal ions was examined after the addition of CQDs. Fluorescence emission occurred when CQDs were added into a blank solution and to the solution containing 12 metal ions, as shown in Fig. 8a and b. However, the fluorescence intensity of CQDs decreased significantly when Cu^{2+} was added, with the fluorescence intensity dropping by 87.1%,

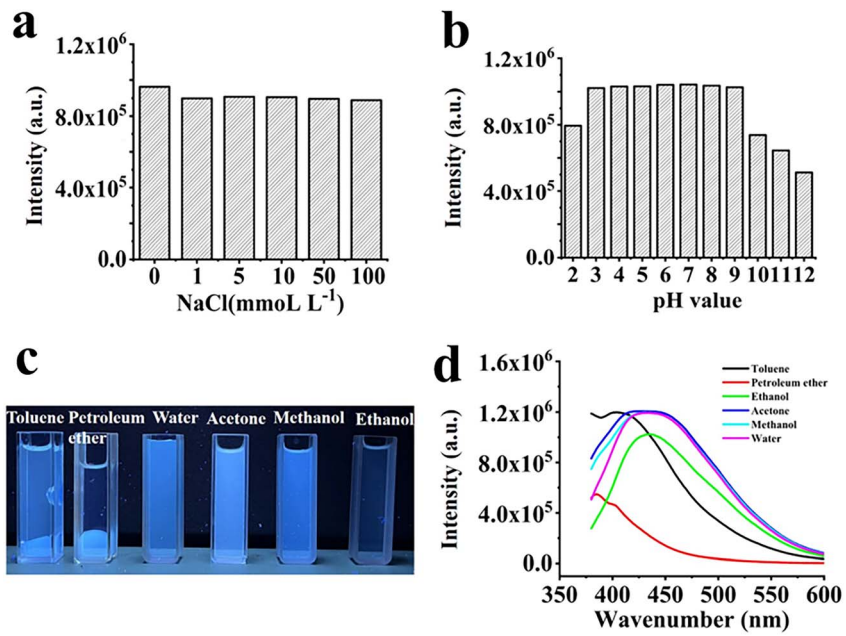

Fig. 7 (a) Fluorescence intensity of CQDs solutions with different NaCl concentrations, (b) fluorescence intensity of CQDs aqueous solution at different pH values, (c) compatibility of CQDs in different solvents, (d) fluorescence intensity of CQDs dissolved in different solvents.

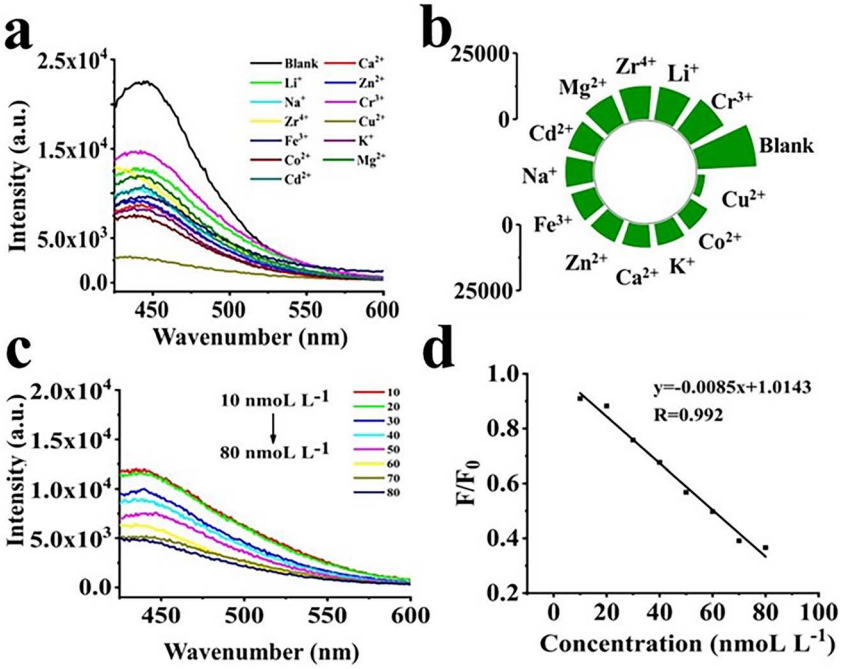

Fig. 8 (a) Fluorescence emission spectra of CQDs with 12 metal ions, (b) fluorescence intensity at 360 nm, (c) fluorescence emission spectra with different concentrations of Cu^{2+}, (d) linear curve for the detection of Cu^{2+}.

indicating that significant fluorescence quenching occurred. As the Cu^{2+} concentration increased from 10 to 80 nM, the fluorescence intensity of the CQDs decreased with increasing Cu^{2+} concentration, as shown in Fig. 8c. The linear correlation coefficient (r) was 0.992 (Fig. 8d). The limit of detection (LOD) was calculated as $3r/S$, where r represents the blank signal standard deviation ($n = 11$), n refers to the number of repeated measurements performed on a blank sample, and S (refers to the slope of the linear curve). Thus, LOD of CQDs for Cu^{2+} was calculated to be 2.83 nmol L^{-1}. A few reported materials could detect two or more metal ions simultaneously. For example, wool keratin-based fluorescent CQDs prepared with nitrogen and sulfur doping could detect Cr^{6+} and Fe^{3+}.[47] In contrast, pigeon dung-synthesized nitrogen and sulfur co-doped fluorescent CQDs could detect $Hg^{2+}$and Fe^{3+}.[48] In our case, the CQDs exhibited a high selectivity for detection of Cu^{2+}. The surface organic groups of CQDs (–COOH and $-NH_2$) have a strong ability to selectively bind with Cu^{2+}, leading to the aggregation of CQDs, which produces a high quenching fluorescence intensity, resulting in the quenching of the fluorescence intensity of CQDs.[49]

The fluorescence intensity showed an excellent linear correlation when the Cu^{2+} concentration was in the range of 10 to 80 nM, as shown in Fig. 8d. After that, we studied the quenching mode and finally determined it to be static quenching. Details of the calculation are presented in the ESI†.[50]

Therefore, the method of CQDs based fluorescence detection was developed and exhibited a wide linear range for quantitative analysis and selective detection of Cu^{2+}. As listed in Table 2, several materials with fluorescence properties have been reported to selectively detect Cu^{2+}. For example, N, S-codoped CQDs (NS-CQDs) were synthesized by a simple one-step hydrothermal process, and detection range of NS-CQDs for Cu^{2+} was 0–12.5 μmol L^{-1} and the LOD was 0.004 μmol L^{-1}.[42] Zhao *et al.*[45] prepared CQDs from lignin for the detection of Cu^{2+}, with a linear range of 0–30 μmol L^{-1} and a LOD of 0.085 nmol L^{-1}. In this study, CQDs prepared from wolfberry stem by hydrothermal method showed better detection ability of Cu^{2+} with linear range of 0.01–0.08 μmol L^{-1} and LOD of 0.0028 μmol L^{-1} than other biomass CQDs.

3.5 Quenching mechanism

Based on current research, several theories have been proposed to explain the fluorescence quenching phenomenon of CQDs, including inner filter effect, electron transfer, and energy

Table 2 A few reported materials for detecting Cu^{2+}

Materials	Methods	LOD (μmol L^{-1})	Linear range (μmol L^{-1})	Ref.
Tea	Ratiometric & colorimetry FL	0.051	0–170	46
Banana	Hydrothermal method	0.004	0–12.5	42
Lignin	Hydrothermal method	0.085	0–30	45
Wolfberry stems	Hydrothermal method	0.0028	0.01–0.08	This work

resonance mechanisms.[51] Zeta potential and UV spectroscopy have been widely utilized to elucidate the quenching mechanism of CQDs.[42] As shown in Fig. S5a,† the Zeta potential of the CQDs solution increased from −24.8 mV to 4.7 mV upon the introduction of Cu^{2+}, indicating the formation of a complex between CQDs and Cu^{2+}. Fig. S5b† demonstrates that the UV absorption spectrum of CQDs underwent a remarkable change at 220 to 270 nm range after the addition of 100 μmol L^{-1} Cu^{2+}, implying a coordination between the functional groups of CQDs and Cu^{2+}.[38] Therefore, it could be inferred that electron transfer between CQDs and Cu^{2+} is the primary cause of fluorescence quenching.

4 Conclusion

Two kinds of carbon-based materials with different properties, AC and CQDs, have been prepared from wolfberry stem waste. Preparation of high specific surface AC after activation with NaOH and an adsorption capacity of 68.06 mg g^{-1} of Cu^{2+}. High adsorption capacity was compared to other biomass AC. The CQDs produce blue emission at 436 nm, which were selective for Cu^{2+} detection and have ultra-LOD (2.83 nmol L^{-1}), Therefore, the preparation of two different performance materials (CQDs and AC) for the detection and removal of heavy metals from the environment by fabrication of waste wolfberry straw not only enables the recycling of waste materials, but also provides a new way of thinking about environmental protection. This "green" and simple preparation method available for CQDs and AC offer a hint for utilization of a variety of waste biomass.

Ethical statement

Not involved for both human and/or animal studies.

Author contributions

Yunjia Xu: investigation, writing – original draft, writing – review & editing. Jingming Lan: writing original draft, methodology, formal analysis, data curation, conceptualization. Baoying Wang: writing original draft, methodology, formal analysis, data curation, conceptualization. Chunmiao Bo: supervision, resources, conceptualization. Junjie Ou: writing–review & editing, supervision, resources, project administration, methodology, investigation, funding acquisition, conceptualization. Bolin Gong: supervision, funding acquisition, conceptualization.

Conflicts of interest

The authors declare that they have no known competing financial interests or personal relationships that could have appeared to influence the work reported in this paper.

Acknowledgements

Financial support is gratefully acknowledged from the National Natural Science Foundation of China (No. 21974137), the CAS-Weigao Research & Development Program ([2017]-009), the Innovation Program of Science and Research from the Dalian Institute of Chemical Physics (DICPI202005) and the National Natural Science Foundation of Ningxia (No. 2021AAC02017) to J. Ou, as well as the National Natural Science Foundation of China (No. 22164001) and the Key research and development program of Ningxia (No. 2022BFE02002) to B. Gong.

References

1 H. Ali, E. Khan and I. Ilahi, Environmental Chemistry and Ecotoxicology of Hazardous Heavy Metals: Environmental Persistence, Toxicity, and Bioaccumulation, *J Chem.*, 2019, 1–14.
2 C. F. Carolin, P. S. Kumar, A. Saravanan, G. J. Joshiba and M. Naushad, Efficient techniques for the removal of toxic heavy metals from aquatic environment: A review, *J. Environ. Chem. Eng.*, 2017, **5**, 2782–2799.
3 V. Antoniadis, S. M. Shaheen, E. Levizou, M. Shahid, N. K. Niazi, M. Vithanage, Y. S. Ok, N. Bolan and J. Rinklebe, A critical prospective analysis of the potential toxicity of trace element regulation limits in soils worldwide: Are they protective concerning health risk assessment? – A review, *Environ. Int.*, 2019, **127**, 819–847.
4 Z. Li, Z. Ma, T. J. van der Kuijp, Z. Yuan and L. Huang, A review of soil heavy metal pollution from mines in China: pollution and health risk assessment, *Sci. Total Environ.*, 2014, **468–469**, 843–853.
5 X. Kan, Y. Dong, L. Feng, M. Zhou and H. Hou, Contamination and health risk assessment of heavy metals in China's lead-zinc mine tailings: A meta-analysis, *Chemosphere*, 2021, **267**, 128909.
6 N. Khalid, M. Aqeel, A. Noman, S. M. Khan and N. Akhter, Interactions and effects of microplastics with heavy metals in aquatic and terrestrial environments, *Environ. Pollut.*, 2021, **290**, 118104.
7 M. Xiang, Y. Li, J. Yang, K. Lei, Y. Li, F. Li, D. Zheng, X. Fang and Y. Cao, Heavy metal contamination risk assessment and correlation analysis of heavy metal contents in soil and crops, *Environ. Pollut.*, 2021, **278**, 116911.
8 H. Qin, T. Hu, Y. Zhai, N. Lu and J. Aliyeva, The improved methods of heavy metals removal by biosorbents: A review, *Environ. Pollut.*, 2020, **258**, 113777.
9 X. Jia, T. Fu, B. Hu, Z. Shi, L. Zhou and Y. Zhu, Identification of the potential risk areas for soil heavy metal pollution based on the source-sink theory, *J. Hazard. Mater.*, 2020, **393**, 122424.
10 S. M. Hosseini, H. Alibakhshi, E. Jashni, F. Parvizian, J. N. Shen, M. Taheri, M. Ebrahimi and N. Rafiei, A novel layer-by-layer heterogeneous cation exchange membrane for heavy metal ions removal from water, *J. Hazard. Mater.*, 2020, **381**, 120884.

11 H. N. Abdelhamid, D. Georgouvelas, U. Edlund and A. P. Mathew, CelloZIFPaper: Cellulose-ZIF hybrid paper for heavy metal removal and electrochemical sensing, *Chem. Eng. J.*, 2022, **446**, 136614.

12 C. Duan, T. Ma, J. Wang and Y. Zhou, Removal of heavy metals from aqueous solution using carbon-based adsorbents: A review, *J. Water Process. Eng.*, 2020, **37**, 101339.

13 B. Barik, A. Kumar, P. S. Nayak, L. S. K. Achary, L. Rout and P. Dash, Ionic liquid assisted mesoporous silica-graphene oxide nanocomposite synthesis and its application for removal of heavy metal ions from water, *Mater. Chem. Phys.*, 2020, **239**, 122028.

14 S. Rajendran, A. K. Priya, P. Senthil Kumar, T. K. A. Hoang, K. Sekar, K. Y. Chong, K. S. Khoo, H. S. Ng and P. L. Show, A critical and recent developments on adsorption technique for removal of heavy metals from wastewater-A review, *Chemosphere*, 2022, **303**, 135146.

15 M. Bilal, J. A. Shah, T. Ashfaq, S. M. Gardazi, A. A. Tahir, A. Pervez, H. Haroon and Q. Mahmood, Waste biomass adsorbents for copper removal from industrial wastewater—a review, *J. Hazard. Mater.*, 2013, **263**(2), 322–333.

16 L. Pan, C. Wang, W. Wu, X. Li, S. Ma, C. Li, Y. Shen and J. Ou, Bioinspired honeycomb-like 3D architectures self-assembled from chitosan as dual-functional membrane for effective adsorption and detection of copper ion, *Micropor Mesopor Mat*, 2022, **335**, 111859.

17 L. Zhu, D. Shen, Q. Liu, C. Wu and S. Gu, Sustainable synthesis of bright green fluorescent carbon quantum dots from lignin for highly sensitive detection of Fe3+ ions, *Appl. Surf. Sci.*, 2021, **565**, 150526.

18 A. I. Licona-Aguilar, A. M. Torres-Huerta, M. A. Dominguez-Crespo, D. Palma-Ramirez, E. Conde-Barajas, M. X. L. Negrete-Rodriguez, A. E. Rodriguez-Salazar and D. S. Garcia-Zaleta, Reutilization of waste biomass from sugarcane bagasse and orange peel to obtain carbon foams: Applications in the metal ions removal, *Sci. Total Environ.*, 2022, **831**, 154883.

19 W. El Malti, A. Hijazi, Z. A. Khalil, Z. Yaghi, M. K. Medlej and M. Reda, Comparative study of the elimination of copper, cadmium, and methylene blue from water by adsorption on the citrus Sinensis peel and its activated carbon, *RSC Adv.*, 2022, **12**, 10186–10197.

20 L. Gu, J. R. Zhang, G. X. Yang, Y. Y. Tang, X. Zhang, X. Y. Huang, W. L. Zhai, E. K. Fodjo and C. Kong, Green preparation of carbon quantum dots with wolfberry as on-off-on nanosensors for the detection of Fe3+ and L-ascorbic acid, *Food Chem.*, 2022, **376**, 131898.

21 R. N. Oss, R. F. Goncalves, S. T. Cassini, M. A. Schettino, D. F. Cipriano and J. C. C. De Freitas, Single step production of activated carbon from microalgae cultivated with urban wastewater, *Algal Res.*, 2022, **64**, 102669.

22 G. M. Kalu-Uka, S. Kumar, A. C. Kalu-Uka, S. Vikram, G. O. Ihekweme, N. Ranjan, E. N. Anosike-Francis, G. Prajapati, A. Nduba, A. P. Onwualu and S. Kumar, Production of Activated Carbon Electrode for Energy Storage Application in Supercapacitors *via* KOH Activation of Waste Termite Biomass, *Waste Biomass Valorization*, 2022, **13**, 2689–2704.

23 A. Alazmi, Synergistic effect of hydrothermal and physical activation approaches to fabricate activated carbon for energy storage applications, *Ceram. Int.*, 2022, **48**, 22131–22140.

24 Z. X. Guan, Z. P. Guan, Z. G. Li, J. H. Liu and K. F. Yu, Characterization and Preparation of Nano-porous Carbon Derived from Hemp Stems as Anode for Lithium-Ion Batteries, *Nanoscale Res. Lett.*, 2019, **14**, 338.

25 A. Alabadi, S. Razzaque, Y. W. Yang, S. Chen and B. Tan, Highly porous activated carbon materials from carbonized biomass with high CO2 capturing capacity, *Chem. Eng. J.*, 2015, **281**, 606–612.

26 J. Liu, D. H. Su, J. R. Yao, Y. F. Huang, Z. Z. Shao and X. Chen, Soy protein-based polyethylenimine hydrogel and its high selectivity for copper ion removal in wastewater treatment, *J. Mater. Chem. A*, 2017, **5**, 4163–4171.

27 S. Y. Gu, C. T. Hsieh, Y. A. Gandomi, Z. F. Yang, L. Y. Li, C. C. Fu and R. S. Juang, Functionalization of activated carbons with magnetic Iron oxide nanoparticles for removal of copper ions from aqueous solution, *J. Mol. Liq.*, 2019, **277**, 499–505.

28 J. P. Chen and S. Wu, Acid/Base-treated activated carbons: characterization of functional groups and metal adsorptive properties, *Langmuir*, 2004, **20**, 2233–2242.

29 X. Y. Gao, L. Wu, Q. Xu, W. Tian, Z. Y. Li and N. Kobayashi, Adsorption kinetics and mechanisms of copper ions on activated carbons derived from pinewood sawdust by fast H3PO4 activation, *Environ. Sci. Pollut. Res.*, 2018, **25**, 7907–7915.

30 T. E. Amoo, K. O. Amoo, O. A. Adeeyo and C. O. Ogidi, Kinetics and Equilibrium Studies of the Adsorption of Copper(II) Ions from Industrial Wastewater Using Activated Carbons Derived from Sugarcane Bagasse, *Int. J. Chem. Eng.*, 2022, 2022.

31 X. L. Xie, H. L. Gao, X. Luo, T. M. Su, Y. Q. Zhang and Z. Z. Qin, Polyethyleneimine modified activated carbon for adsorption of Cd(II) in aqueous solution, *J. Environ. Chem. Eng.*, 2019, **7**, 103183.

32 Q. H. Guo, Z. Y. Zang, J. Ma, J. Y. Li, T. Zhou and R. P. Han, Adsorption of copper ions from solution using xanthate wheat straw, *Water Sci. Technol.*, 2020, **82**, 2029–2038.

33 L. Wu, Z. S. Shang, H. Wang, W. J. Wan, X. Y. Gao, Z. Y. Li and N. Kobayashi, Production of activated carbon from walnut shell by CO_2 activation in a fluidized bed reactor and its adsorption performance of copper ion, *J. Mater. Cycles Waste Manage.*, 2018, **20**, 1676–1688.

34 P. Devi, P. Rajput, A. Thakur, K. H. Kim and P. Kumar, Recent advances in carbon quantum dot-based sensing of heavy metals in water, *TrAC, Trends Anal. Chem.*, 2019, **114**, 171–195.

35 N. Q. Gong, H. Wang, S. Li, Y. L. Deng, X. A. Chen, L. Ye and W. Gu, Microwave-Assisted Polyol Synthesis of Gadolinium-Doped Green Luminescent Carbon Dots as a Bimodal Nanoprobe, *Langmuir*, 2014, **30**, 10933–10939.

36 Y. Y. Meng, Y. Zhang, W. Y. Sun, M. Wang, B. L. He, H. Y. Chen and Q. W. Tang, Biomass converted carbon quantum dots for all-weather solar cells, *Electrochim. Acta*, 2017, **257**, 259–266.

37 G. K. Hu, L. Ge, Y. Y. Li, M. Mukhtar, B. Shen, D. S. Yang and J. G. Li, Carbon dots derived from flax straw for highly sensitive and selective detections of cobalt, chromium, and ascorbic acid, *J. Colloid Interface Sci.*, 2020, **579**, 96–108.

38 S. O. Sanni, T. H. G. Moundzounga, E. O. Oseghe, N. H. Haneklaus, E. L. Viljoen and H. G. Brink, One-Step Green Synthesis of Water-Soluble Fluorescent Carbon Dots and Its Application in the Detection of Cu2+, *Nanomaterials*, 2022, **12**, 958.

39 P. Chauhan, S. Dogra, S. Chaudhary and R. Kumar, Usage of coconut coir for sustainable production of high-valued carbon dots with discriminatory sensing aptitude toward metal ions, *Mater. Today Chem.*, 2020, **16**, 100247.

40 X. H. Sun, J. He, S. H. Yang, M. D. Zheng, Y. Y. Wang, S. Ma and H. P. Zheng, Green synthesis of carbon dots originated from Lycii Fructus for effective fluorescent sensing of ferric ion and multicolor cell imaging, *J. Photochem. Photobiol., B*, 2017, **175**, 219–225.

41 L. L. Zhu, D. K. Shen, Q. Liu, C. F. Wu and S. Gu, Sustainable synthesis of bright green fluorescent carbon quantum dots from lignin for highly sensitive detection of Fe3+ ions, *Appl. Surf. Sci.*, 2021, **565**, 150526.

42 N. Chaudhary, P. K. Gupta, S. Eremin and P. R. Solanki, One-step green approach to synthesize highly fluorescent carbon quantum dots from banana juice for selective detection of copper ions, *J. Environ. Chem. Eng.*, 2020, **8**, 103720.

43 X. Wang, P. Yang, Q. Feng, T. T. Meng, J. Wei, C. Y. Xu and J. Q. Han, Green Preparation of Fluorescent Carbon Quantum Dots from Cyanobacteria for Biological Imaging, *Polymers*, 2019, **11**, 616.

44 Y. S. Liu, Y. A. Zhao and Y. Y. Zhang, One-step green synthesized fluorescent carbon nanodots from bamboo leaves for copper(II) ion detection, *Sens. Actuators, B*, 2014, **196**, 647–652.

45 Y. S. Zhao, S. S. Jing, X. W. Peng, Z. H. Chen, Y. J. Hu, H. Zhuo, R. C. Sun and L. X. Zhong, Synthesizing green carbon dots with exceptionally high yield from biomass hydrothermal carbon, *Cellulose*, 2020, **27**, 415–428.

46 Y. P. Hu, J. Yang, J. W. Tian, L. Jia and J. S. Yu, Waste frying oil as a precursor for one-step synthesis of sulfur-doped carbon dots with pH-sensitive photoluminescence, *Carbon*, 2014, **77**, 775–782.

47 Y. Y. Song, N. Qi, K. Li, D. Cheng, D. Wang and Y. Li, Green fluorescent nanomaterials for rapid detection of chromium and iron ions: wool keratin-based carbon quantum dots, *RSC Adv.*, 2022, **12**, 8108–8118.

48 Q. H. Ye, F. Y. Yan, Y. M. Luo, Y. Y. Wang, X. G. Zhou and L. Chen, Formation of N, S-codoped fluorescent carbon dots from biomass and their application for the selective detection of mercury and iron ion, *Spectrochim. Acta, Part A*, 2017, **173**, 854–862.

49 J. R. Bhamore, S. Jha, T. J. Park and S. K. Kailasa, Fluorescence sensing of Cu2+ ion and imaging of fungal cell by ultra-small fluorescent carbon dots derived from Acacia concinna seeds, *Sens. Actuators, B*, 2018, **277**, 47–54.

50 R. Yang, X. F. Guo, L. H. Jia, Y. Zhang, Z. L. Zhao and F. Lonshakov, Green preparation of carbon dots with mangosteen pulp for the selective detection of Fe3+ ions and cell imaging, *Appl. Surf. Sci.*, 2017, **423**, 426–432.

51 Y. Mu, Q. Zhuang, S. Huang, M. Hu, Y. Wang and Y. Ni, Adenine-stabilized carbon dots for highly sensitive and selective sensing of copper(II) ions and cell imaging, *Spectrochim. Acta, Part A*, 2020, **239**, 118531.